

# An efficient multiscale model of damping properties for filled elastomers with complex microstructures

John A. Moore<sup>a</sup>, Ruizhe Ma<sup>a</sup>, August G. Domel<sup>a</sup>, Wing Kam Liu,<sup>a,1,\*</sup>

<sup>a</sup>*Department of Mechanical Engineering, Northwestern University, 2145 Sheridan Road, Evanston, IL 60208-3111, USA*

---

## Abstract

This work proposes an efficient framework for prediction of filled elastomer damping properties based on imaged microstructures. The efficiency of this method stems from a hierarchical multi-scale modeling scheme, in which the constitutive response of subcell regions, smaller than a representative volume element (RVE), are determined using micromechanics; the resulting constitutive parameters then act as inputs to finite element simulations of the RVE. It is shown that the micromechanics models of Halpin-Tsai and Mori-Tanaka are insufficient for modeling subcells with many filler clusters, and thus these models are augmented by an additional interaction term, based on stress concentration factors. The multiscale framework is verified in two dimensions and extended to predictions for three dimensional systems, which include the response of matrix-filler interphase properties. The proposed multiscale framework shows a significant improvement in computational speed over direct numerical simulations using finite element analysis, and thus the proposed framework allows for detailed parametric studies of microstructural properties to aid in the design of filled elastomeric systems.

*Keywords:* A. Particle-reinforcement, B. Mechanical properties, C. Micro-mechanics, C. Computational modeling, Imaged-based modeling

---

---

\*Corresponding author

*Email address:* [w-liu@northwestern.edu](mailto:w-liu@northwestern.edu) (Wing Kam Liu,)

<sup>1</sup>Adjunct Professor under the Distinguished Scientists Program Committee at King Abdulaziz University (KAU), Jeddah, Saudi Arabia

## 1. Introduction

Filled elastomers have found many applications in a variety of fields spanning the automotive [1] [2], civil engineering [3] [4] and even food packing industries [5]. In many applications polymers provide desirable damping or energy dissipation properties but can lack the strength needed to carry structural loads or resist wear. The addition of fillers add strength to polymer systems but can reduce damping properties. Wang [2] gives a specific example where it is shown that the *wet grip* of tires is improved by increasing damping property values at room temperature. The addition of strengthening fillers, however, acts against these wet grip improvements by decreasing room temperature damping values. Thus, as damping decreases, performance decreases as well, creating a design dilemma, trading performance with strength.

A powerful tool to aid in this design decision would be one that could accurately predict the damping properties of an existing material while simultaneously allowing for parametrized studies of new virtual materials. This model would allow a designer to determine if a material meets both the strength and damping goals before the material is produced and to gage what modifications are needed before production. Such a model is the goal of this work. This model will be based on the premise that knowledge of the three dimensional (3D) morphology of a filled system (for example from sectioned scanning electron microscopy) is key to accurate computational models. The major challenge to be addressed is that direct numerical simulations (DNS) using computational tools such as molecular dynamics or the finite element method (FEM) can be prohibitively slow if not intractable when modeling a 3D microstructure on the scale of a representative volume element (RVE). Thus, a multiscale approach is proposed here using micromechanics to homogenize the morphology of sub-RVE scale subcells. A coarse finite element model is then used to simulate the combined response of these subcells, resulting in a reduced computation size as compared to DNS of the entire microstructure. While a homogenized model cannot account for all of the information included in direct simulations, the advantage in computational speed will be substantial, making it a powerful tool for materials design of filled elastomer systems.

Section 2 will outline previous micromechanical models and image based modeling. The material properties used in each simulation will be given in Section 3. Section 4 will describe both the finite element implementation as well as the multiscale modeling scheme. The sub-RVE mechanisms affecting damping will be explored in Section 5. Section 6 will pose an extension to existing micromechanics models to capture these sub-RVE mechanics. The implementation of such a model

in two dimensions (2D) and results are shown in Section 7 and compared to DNS to verify the model. Once verified, the model is used to predict the response of a 3D microstructure in Section 8. The effects of an interphase region are then explored for a 3D system in Section 9. Finally, conclusions are drawn in Section 10 and extensions are posed for future modeling and materials design.

## 2. Background

Two micromechanics models are popular for representing the effective stiffness of a filled composite and will form the basis for the proposed work. These are the Mori-Tanaka [6] and Halpin-Tsai [7] models. Both take into account the interaction between filler particles. To illustrate the nature of this interaction, the framework of each of these models will be briefly outlined. The formulation of each theory can be understood by first considering a series of inclusions with stresses and strains characterized by Eshelby's solution [8](as described in [9]). The composite properties which encompass both the effect of inclusions and the surrounding matrix are then given by fourth order stiffness tensor  $\bar{\mathbf{L}}$ . The value of  $\bar{\mathbf{L}}$  can be determined by postulating a matrix strain  $\hat{\boldsymbol{\varepsilon}}$  and stiffness properties  $\hat{\mathbf{L}}$  for a region directly surrounding each inclusion. The assumptions regarding these strain and stiffness values are often what distinguish one micromechanical model from another. For instance, if  $\hat{\mathbf{L}}$  is defined as the matrix properties  $\mathbf{L}_0$ , and  $\hat{\boldsymbol{\varepsilon}}$  as the average strain  $\bar{\boldsymbol{\varepsilon}}$  of the total body, then a dilute approximating is found, which is simply a sum of several traditional Eshelby solutions for each inclusion. If  $\hat{\mathbf{L}}$  is defined as the matrix properties  $\mathbf{L}_0$  and  $\hat{\boldsymbol{\varepsilon}}$  as the average strain in the matrix alone,  $\bar{\boldsymbol{\varepsilon}}_0$ , then the Mori-Tanaka stiffness tensor is found. The Mori-Tanaka stiffness tensor is given as

$$\bar{\mathbf{L}}^{MT} = \mathbf{L}_0 + \sum_{r=1}^N c_r (\mathbf{L}_r - \mathbf{L}_0) \mathbf{T}_r \left[ c_0 \mathbf{I} + \sum_{n=1}^N c_n \mathbf{T}_n \right]^{-1}, \quad (1)$$

where  $c_0$  is the volume fraction of matrix material,  $c_r$  is the volume fraction of phase  $r$ ,  $\mathbf{I}$  is a fourth order identity tensor,  $N$  is the number of distinct inclusion phases, and

$$\mathbf{T}_r = \left[ \mathbf{I} + \mathbf{S}_r \mathbf{L}_0^{-1} (\mathbf{L}_r - \mathbf{L}_0) \right]^{-1}. \quad (2)$$

Where the Eshelby tensor  $\mathbf{S}_r$  is a function of  $\mathbf{L}_0$  and  $\bar{\boldsymbol{\varepsilon}}_0$ . Finally, if  $\hat{\mathbf{L}}$  is chosen to be the average composite properties  $\bar{\mathbf{L}}$ , and  $\hat{\boldsymbol{\varepsilon}}$  is chosen as the average total strain  $\bar{\boldsymbol{\varepsilon}}$  then a self consistent approximation is formed; in that, the self consistent stiffness tensor  $\bar{\mathbf{L}}^{SC}$  is expressed as a function of

itself. Many approaches [7] solve for specific cases of  $\bar{\mathbf{L}}^{SC}$ . The Halpin-Tsai equations simplify the self consistent approaches of Hermans [10] and Hill [11] resulting in the following expression for composite Young's modulus [7],

$$\frac{\bar{E}_{yy}}{E_m} = \frac{1 + 2\mathcal{R}c_f\eta}{1 - c_f\eta} \quad (3)$$

$$\eta = \frac{(E_f/E_m) - 1}{(E_f/E_m) + 2\mathcal{R}} \quad (4)$$

where  $\mathcal{R}$  is the aspect ratio of the inclusion particle in two dimensions (i.e.  $L/t$  where  $L$  is the particle length and  $t$  the particle thickness,  $L$  being in the direction of loading  $y$ ),  $c_f$  is the filler volume fraction,  $E_m$  is the Young's modulus of the polymer matrix,  $E_f$  the Young's modulus of the filler particles and  $E_{yy}$  the longitudinal Young's modulus of the composite system. In the determination of Equations 3 and 4 a number of assumptions were made. Of note were the assumption that the composite modulus is independent of matrix Poisson's ratio and that all filler particles are uniaxially aligned and identical [10]. Also, the term  $2\mathcal{R}$  used in Equation 3 and 4 was determined through comparison with available finite element results [10].

It can be shown from the above formulation that the Mori-Tanaka model and the self consistent theory (on which Halpin-Tsai model is based) both account for the interaction of filler inclusions. Mori-Tanaka assumes that the strain in a given inclusion can be determined using the average matrix strain,  $\bar{\epsilon}_0$  which differs from the average total strain. This difference is attributed to the presence of the other inclusions. Thus, a single inclusion's response is a function of all other inclusions. Self-consistent theory makes a similar assumption, that the inclusions stress is a function of the average bulk properties  $\bar{\mathbf{L}}$  resulting again in a single inclusion's response being a function of all other inclusions. This shows that both models allow for a single inclusion's stress to be altered by the presence of other inclusions and thus, an interaction between inclusions is modeled. The author will define this as a *weak* interaction, in that, the explicit increase in stress due to a pair or group of inclusions is not modeled. The extensions proposed in Section 6 will attempt to capture a *strong* interaction between inclusions by modeling stress risers based on the influence of adjacent fillers.

The application of these models to viscoelasticity is achieved by using the elastic-viscoelastic correspondence principle. The details of which are given in the work of Brinson et al. [12]. In short, an elastic modulus, such as Young's modulus, can be viewed as complex and a function of

frequency,  $\omega$ .

$$E^*(\omega) = E'(\omega) + iE''(\omega), \quad (5)$$

where  $E'$  and  $E''$  are the storage and loss modulus respectively and  $i = \sqrt{-1}$ . Where  $E'$  represents the elastic response in-phase with the strain loading and  $E''$  represents the response 90 degrees out-of-phase with the loading due to time dependent viscoelastic effects. The ratio of the loss to storage modulus will be referred to here as  $\tan \delta$  (where  $\delta$  is the phase lag of the material) and is proportional to the energy dissipation or damping of the system [2].

$$\tan \delta = \frac{E''}{E'} \quad (6)$$

This value can be directly related to properties of importance to many engineering applications and thus this work will focus on determining  $\tan \delta$  for a filled elastomer. Using Equation 3 and Equation 4 and assuming a linear elastic filler model, Halpin-Tsai can be written in a complex form, where  $E_{yy}^*$  and  $E_m^*$  are functions of frequency, as

$$\frac{\bar{E}_{yy}^*}{E_m^*} = \frac{1 + 2\mathcal{R}c_p\eta^*}{1 - c_f\eta^*} \quad (7)$$

$$\eta^* = \frac{(E_f/E_m^*) - 1}{(E_f/E_m^*) + 2\mathcal{R}} \quad (8)$$

from which  $\tan \delta$  can be determined. Likewise, if a complex Poisson's ratio is given as  $\nu^*$  and only two phases are considered, then  $E^*$  and  $\nu^*$  of the matrix and filler can be determined by inserting the complex forms of  $\mathbf{S}_r^*$ ,  $\mathbf{L}_r^*$  and  $\mathbf{L}_0^*$  into Equation 1, resulting in a complex Mori-Tanaka stiffness tensor [12], given by

$$\bar{\mathbf{L}}^{*,MT} = \mathbf{L}_m^* + c_f(\mathbf{L}_f^* - \mathbf{L}_m^*)\mathbf{T}_f^*[c_m\mathbf{I} + c_f\mathbf{T}_f^*]^{-1}, \quad (9)$$

where  $\mathbf{T}_f^*$  is the complex form of Equation 2 evaluated using the material properties of the filler. Brinson et al. [12] have studied  $\bar{\mathbf{L}}^*$  using Mori-Tanaka and have shown good agreement with finite element simulations of a periodic computational unit cells with a single inclusion. Brinson's work, however, was not intended to model larger cells with many interacting inclusions. Putz et al. [13] used the complex form of the Halpin-Tsai expression to compare to experimental data for carbon nanotube filled composites, but no work was done to remedy discrepancies between the model and experiments.

A number of works have included a region of modified properties between the filler and matrix, known as the interphase region (or IP region), into micromechanical models. Ji [14] proposed a three phase model for composite stiffness. This model accounted for a linear gradient in matrix properties near fillers and agreed well with experimental data for polystyrene/cloisite 10A nanocomposites [1]; however, these results were determined by fitting a number of parameters in the model to agree with experimental findings [1]. The model was also limited to random filler microstructures and was not applied to viscoelastic responses. Three phase micromechanics models, including Ji's model, along with self consistent models, such as [15] which include a particle coating phase, are intended for randomly dispersed filler particles and do not account for a strong interaction between closely grouped particles. Gusev and Lurie [16] used a four phase model of spherical filler particles to predict  $\tan \delta$  for ordered and random microstructures. The four phase model and detailed finite element simulations agreed well when only the two interphase regions were considered viscoelastic (the matrix and fillers were considered elastic), and a single frequency of 1 rad/sec was studied. Gusev also observed that the results from ordered and random microstructures showed very similar trends. From this observation they concluded that the effective properties of composites with low aspect ratio fillers lack a strong sensitivity to micro-structural variations, thus accounting for the effectiveness of the four phase model. The present work will show that for arbitrary shaped fillers with viscoelastic matrix properties, considered over a range of frequencies, microstructure plays a more prominent role, and thus it is expected, that the four phase model of Gusev may prove less effective. H. Liu and Brinson [17] have also carried out detailed finite element analysis to inform models of IP effects. Brinson numerically computed a strain concentration tensor for various inclusion geometries, such as nanotubes and nanoplates. This analysis requires a specific finite element analysis for all filler geometries and thus may become computationally expensive for arbitrarily complex microstructures. A similar approach was employed by Song et al. [18]. This model introduced a scalar strain amplification factor pre-multiplying the complex matrix modulus of a filled system. The amplification factor was expressed in an semi-empirical form accounting for a number of microstructural parameters but on some empirical factors in order to match experimental data.

The model presented here will be capable of including IP effects but will first focus on computing mechanics of a sub-RVE cell containing many interacting filler particles. Then the IP properties will be added for a 3D demonstration. The model will rely on extracting data from a microstructural

image. This image is broken down into binary voxels which represent either matrix or filler and are illustrated in Figure 1. A recent work by Mishnaevsky [19] used voxel based images such as

	a	b	c	d
A	Matrix			
B			Filler	
C				
D				

Figure 1: voxel representation of microstructure

in Figure 1 combined with micromechanics. Mishnaevsky’s approach was to extract the volume fraction of the voxel columns (i.e. a-d Figure 1) and determine the stiffness of each using an isostress Reuss model. The combined (composite) response of all columns was then calculated using a Voigt (isostrain) model. Through this approach  $\bar{E}$  can be quickly calculated for arbitrarily complex microstructures. This work was not extended to viscoelastic properties. The simulation results were able to match experimental trends when modulus was compared to weight content of nanoclays but failed to match the slope and magnitude of such a curve.

The work of Deng et al. [20] used this voxel representation to determine the interphase properties of a filled polymer system by comparing finite element analysis of a 2D, 300 x 300 voxel, reconstructed image to experimental results. This work was extended to 3D in the study by Breneman et al. [21]. For both of these works interphase thickness was limited to integer multiples of the mesh size. The proposed model will speed up the voxel based calculations of Deng et al. and Breneman et al. and also allow for more flexibility in interphase thickness modeling.

The work shown here uses both Mori-Tanaka and Halpin-Tsai models extended to capture *strong* interactions between particles (and IP in 3D) and will also capture arbitrarily complex structures through the voxel representations.

### 3. Material Properties

In this work, elastomeric polymers with stiff fillers will be addressed. Examples of polymer/matrix materials are styrene-butadienes [2] or ethylene-propylenes [18], while examples of fillers are carbon black or silica [2]. A viscoelastic polymer with frequency dependent properties will be used for the matrix. Values of matrix properties  $E'_m$  and  $E''_m$  used in this work are based on the *soft material*  $\tan \delta_m$  studied by Brinson and Lin [12]. The values of  $E'_m$  and  $E''_m$  and  $\tan \delta_m$  are shown as a functions of frequency in Figure 2. The polymer matrix is considered nearly in-

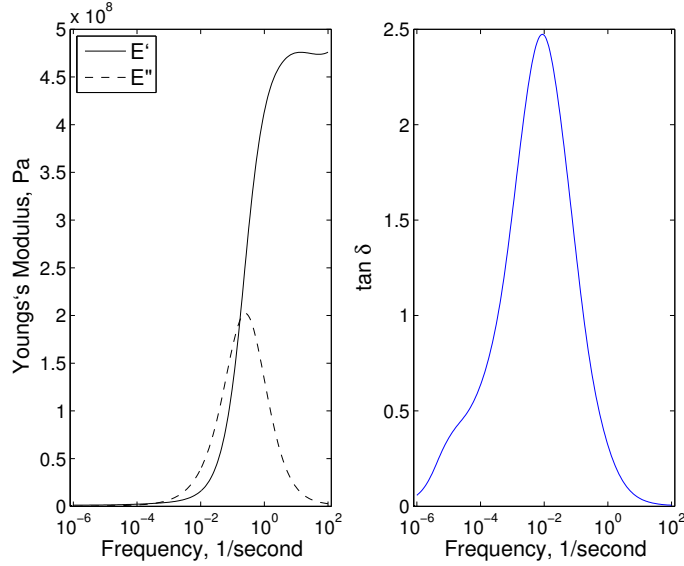


Figure 2: Material properties of matrix based on data from [12]

compressible with a Poisson's ratio of  $\nu_m = 0.48$ . The density of both phases is considered small ( $\rho_m = \rho_f = 1 \times 10^{-9} \text{ kg/m}^3$ ) to avoid any inertial effects in finite element analysis which are absent in micromechanical modeling and negligible in dynamic mechanical analysis (DMA) testing used to characterize viscoelastic properties. The filler is considered to be stiff as compared to the matrix and of a brittle nature. Thus, the filler is considered to have  $E_f = 1 \times 10^9 \text{ Pa}$ . A filler Poisson's ratio of  $\nu_f = 0.4$  is used in this work based on the value used in [20]. The values of  $E_f$  and  $\nu_f$  are considered frequency independent.



#### 4. Finite Element Model

Finite element modeling will be used for two purposes in this work. First, as a verification tool for both subcell and cell models, and second, as an RVE level simulation tool of the cell (see Figure 3). The properties of an RVE are defined in the Micromechanics text [9]. For this work an

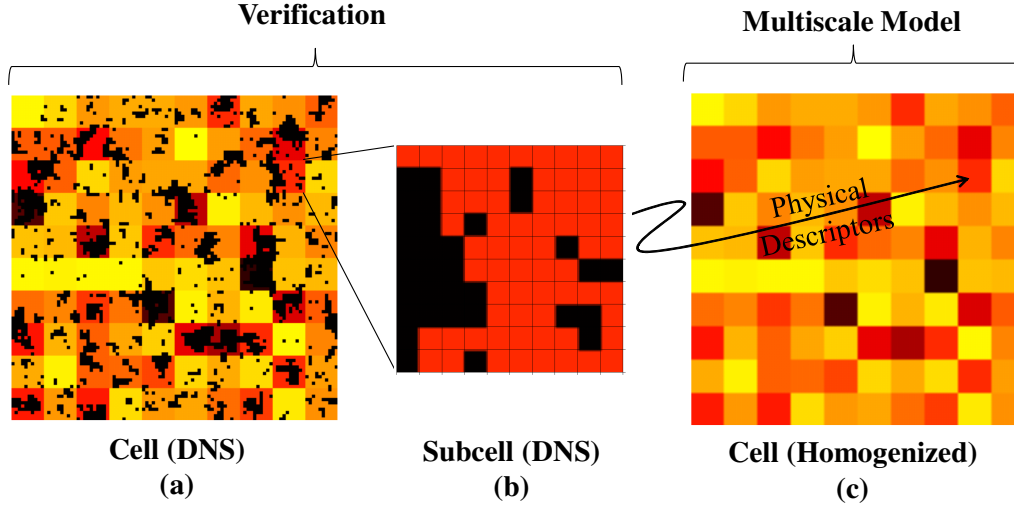


Figure 3: a) 2D voxel model of cell, colors represent volume fraction of subcell region b) 10x10 subcell used for DNS verification and to determine physical descriptors as input to the homogenized cell model c) homogenized cell model colors represent different material properties

RVE cell (Figure 3a) is broken down into subcells (Figure 3b); each subcell's average constitutive properties are then calculated using micromechanics. A coarse finite element mesh of the cell is then created with each element representing a subcell (Figure 3c). The result is a hierarchical multiscale modeling procedure. This procedure recognizes that the response of each subcell will differ from other subcells and from the response of the RVE as a whole (if this was not true then the subcell would be considered the RVE). Thus, the cell finite element model allows for strain inhomogeneities within an RVE by allowing each element to have different material properties based on each subcell's microstructure.

The FEM models used to verify subcell calculations and the FEM models used to simulate the RVE cell will employ the same boundary conditions and finite element formulations; only the meshes will differ between the subcell and cell. Both the subcell and cell models will use the

following assumptions. The boundary conditions shown in Figure 4 will be used. The right edge of

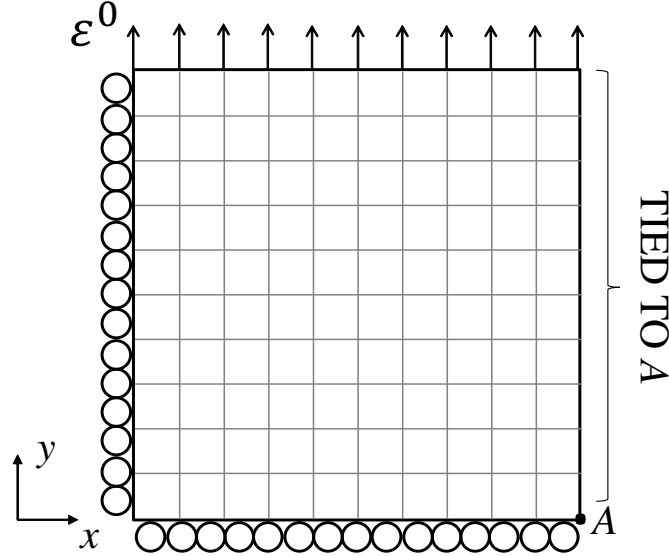


Figure 4: Example boundary conditions and mesh, circles represent roller supports and  $\epsilon^0$  is a uniform applied strain

the mesh in Figure 4 is tied to node  $A$  in the  $x$ -direction such that the right edge remains straight. This constraint forces periodic stress boundary conditions on the model which account for Poisson's effect. In 2D, a plane strain assumption will be used to model the subcell/cell as a piece of a much larger bulk of material. A displacement resulting in an applied strain of  $\epsilon^0$  is applied in the  $y$ -direction as shown in Figure 4. The FEM analysis will be linear; thus, the magnitude of  $\epsilon^0$  will have a linear effect. While an applied strain of  $\epsilon_{yy}^0 = 1.0 + 0.0i$  is assumed, this value is somewhat arbitrary because responses from other applied small strains can be linearly scaled from this result, and the composite values of  $E'$ ,  $E''$  and  $\tan \delta$  are independent of the real value of  $\epsilon_{yy}^0$ .

To account for the nearly incompressible nature of the matrix, hybrid four node quadrilateral elements are used in 2D to avoid numerical locking [22] (see Abaqus manual for more details [23]). Hybrid eight node bricks are used in 3D. Finally, the matrix and fillers are considered perfectly bonded. The interface nodes between each phase are concurrent, and no contact or multiple point constraint are used to connect the phases. Three example meshes are shown in Figure 5. Figure 5a is a subcell mesh based on voxel representations, 5b is a subcell mesh for a single particle and

5c is the coarse homogenized mesh in 2D. Again the reader is reminded that 5a and 5b are for verification only, where as 5c is used as part of the multiscale model.

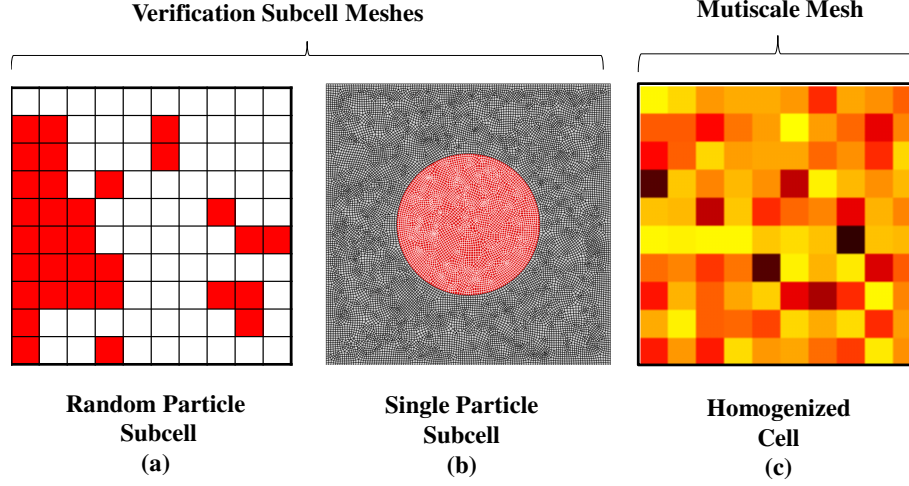


Figure 5: a) uniform subcell mesh with random filler particles b) fine mesh of single particle c) coarse mesh of homogenized cell

## 5. Subcell Mechanisms

The model extension presented in Section 6 is based on the mechanics of a subcell. The goal is that such a model can represent both single filler particle and multiple filler particles (as in Figure 5a-b). The power of the model will be that it can represent a subcell much larger than a single filler particle, which leads to fewer homogenized subcells and thus a fast cell model. It is also a goal that the model extension be rooted in the subcell mechanics such that phenomenological fitting parameters are avoided as much as possible.

To motivate such a model, two types of subcell structures were studied by DNS using the FEM. The two types of structures are: a single filler particle and random particles. A subcell containing a single particle can be viewed as the smallest useful subcell. A subcell containing random particles can be viewed as a much largest subcell where clusters appear to be single points. Alternatively, a subcell containing a single particle can be viewed as the most ordered and periodic structure while a subcell containing random particles can be viewed as the most disordered and random.

Using the FEM model shown in Figure 5b, the peak value of  $\tan \delta$  for a number of filler volume fractions are shown in Figure 6. The average response of 100 random subcells (see Figure 5a)

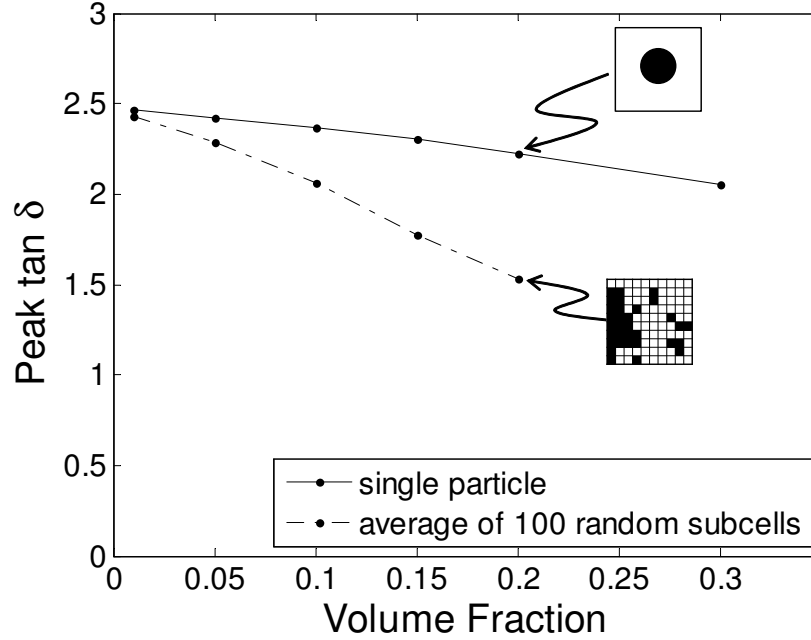


Figure 6: peak  $\tan \delta$  values for single particles subcells and the average peak  $\tan \delta$  values of 100 random particles subcells (100 subcells per volume fraction)

for varying volume fractions are also plotted. It can be seen that the viscoelastic response differs greatly between the random cluster and single particle subcells. The magnitude of the real stress response for an random subcell and a single particle subcell are shown in Figure 7. This figure highlights that there is a strong interaction between the two particles near the right-hand-side of Figure 7b, represented by regions of high stress. The interaction is much weaker in Figure 7b <sup>2</sup>. A model of the strong interaction in Figure 7b will be discussed in the next section. Based on Figure 7, along with the study of the response of many other subcells with random clusters, it is concluded that the interaction between particles is a large contributor to the discrepancy between the random

<sup>2</sup> the high stress region spanning to the edge in 7a is an interaction with the particle in the neighboring subcell, due to periodic boundary conditions

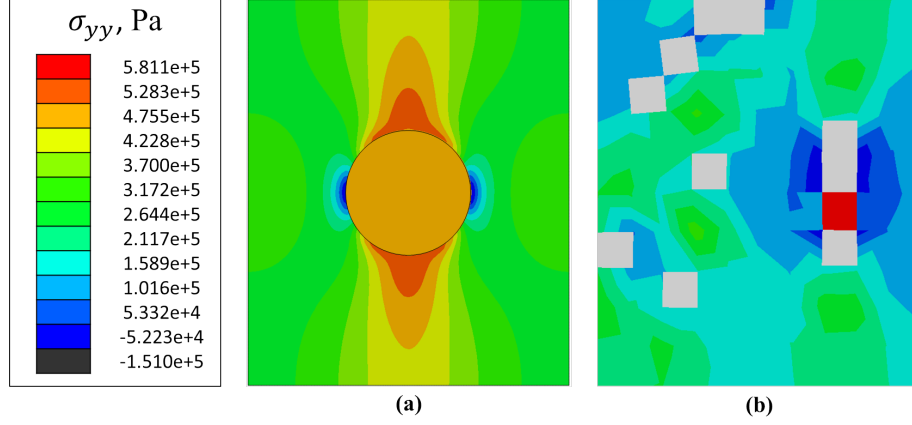


Figure 7: Real normal stress in the  $y$  for a single particle and random particles both at 10% volume fraction. Both contours are at a frequency of  $1 \times 10^{-2}$  (1/second). The light grey areas in the random structure are particles where the stress contour has been removed for comparison of matrix stress.

cluster and single particle responses shown in Figure 6. Thus, the forthcoming model extension will account for the level of particle interaction as a descriptor which has a strong effect on  $\tan \delta$ .

Turning now to the micromechanics models, two descriptors are shown to affect subcell response: volume fraction and aspect ratio of the filler particles. Figure 8 shows  $\tan \delta$  predictions using both the Mori-Tanaka and Halpin-Tsai models, in 2D, for a particle with aspect ratio of 1.0 and varying volume fractions. It can be seen from Figure 8 that volume fraction has a strong effect on both the peak value of  $\tan \delta$  and the frequency of the peak. The frequency of the peak moves to a lower frequency range as volume fraction increases. Mori-Tanaka predictions of peak  $\tan \delta$  are slightly higher at low volume fractions and lower at high volume fractions. Overall, it is shown that both micromechanics models predict similar values for  $\tan \delta$  at a given volume fraction with a constant aspect ratio. The aspect ratio is then varied for each model and the effect is shown in Figure 9. It can be seen that each model shows different responses at high aspect ratios. Halpin-Tsai predicts a double peaked  $\tan \delta$  at high aspect ratio while Mori-Tanaka predicts only a slight asymmetry due to aspect ratio. Halpin-Tsai is more sensitive to aspect ratio than Mori-Tanaka. The type of clusters considered in this work are relatively compact ( $\mathcal{R} = 1$  to 3); thus, the effect of aspect ratio on  $\tan \delta$  will be smaller than that of volume fraction and particle interaction but will still be considered. To conclude, the three main physical descriptors of the subcell, which will inform the micromechanics model extension, are:

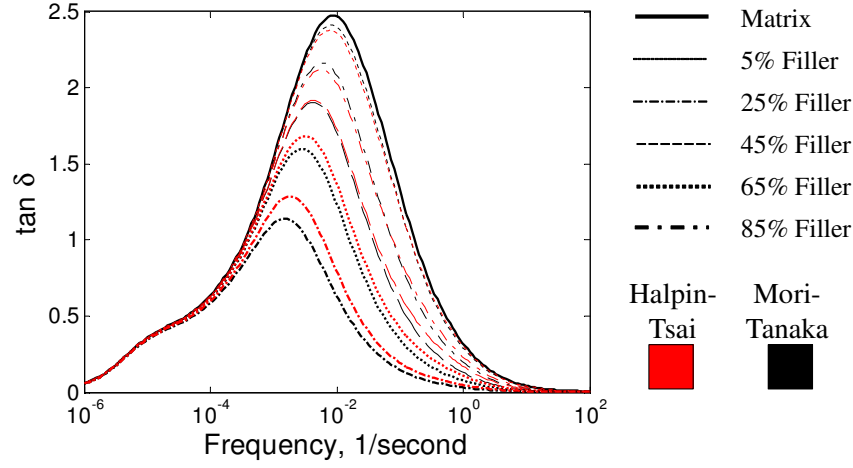


Figure 8:  $\tan \delta$  predictions for 2D systems with aspect ratios of 1.0 at varying volume fractions base on Halpin-Tsai(red) and Mori-Tanaka(black) models

- volume fraction of filler particles
- percentage of filler particles interacting
- aspect ratio of filler particles.

## 6. Micromechanics Model

To begin the development of a micromechanical model extension, it is first observed that results from the complex versions of Halpin-Tsai and Mori-Tanaka models agree quite well with DNS of a

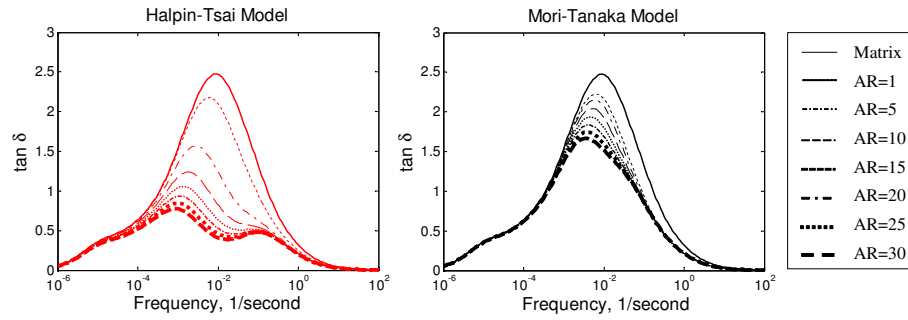


Figure 9:  $\tan \delta$  predictions for 2D systems with volume fractions of 0.20 at varying aspect ratio base on Halpin-Tsai(red) and Mori-Tanaka(black) models

single particle with volume fractions less than less than 30%, as shown in Figure 10. Thus, the model

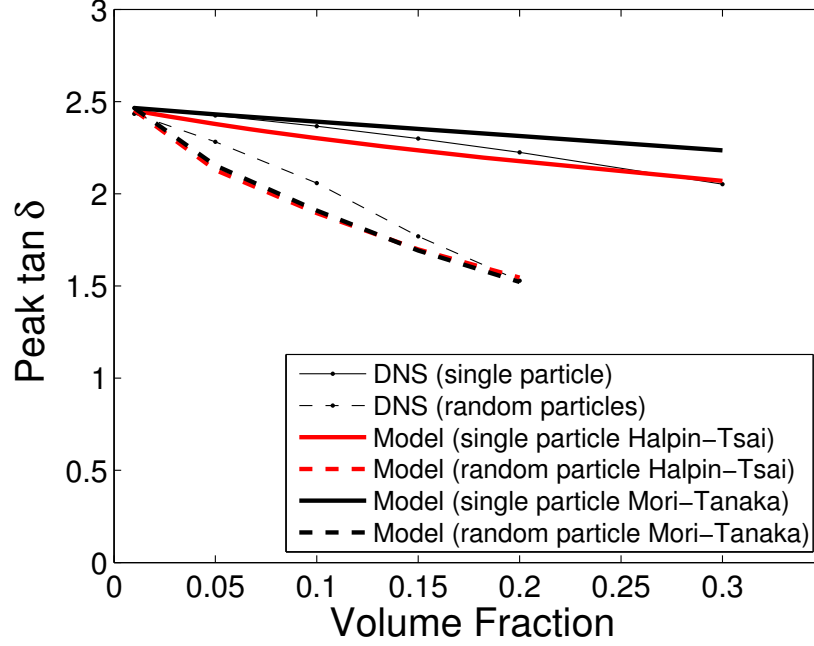


Figure 10: comparison of DNS peak  $\tan \delta$  results to the predictions made using the model extension and the two base models, Halpin-Tsai(red) and Mori-Tanaka(black)

extension will extend either Mori-Tanaka or Halpin-Tsai in such a way that if a subcell encloses only a single cluster, then the model extension degrades to the base model (either Mori-Tanaka or Halpin-Tsai). The second note on the forthcoming model extension is that it will not address the exact mechanisms at every point in the subcell but will rather model the average response. To that means, the model will carry less information than detailed simulations but also with much less computationally expensive.

The extension of Mori-Tanaka or Halpin-Tsai starts with the average stress predicted by these models,  $\sigma^b$ . This will be called the stress of the base model (given by the superscript  $b$ ). It is then postulated that a region of the matrix has a higher stress than  $\sigma^b$ , which is due to the interaction of filler particles. The average stress in this *interaction* region will be denoted as,  $\sigma^{int}$ . The volume fraction of this elevated stress region is denoted as  $w_1$ . The base and interaction stresses

are combined using the following rule-of-mixtures type breakdown of stress

$$\bar{\sigma} = (1 - w_1)\sigma^b + w_1\sigma^{int}. \quad (10)$$

The next step is to formulate an expressions for  $\sigma^{int}$ . To determine the interaction stress, it is postulated that there is a region of the matrix with an elevated stress given by

$$\sigma^{int} = K_t^* \sigma^b, \quad (11)$$

where  $K_t^*$  is the complex version of the traditional tensile stress concentration factor. Equation 11 assumes that each filler is surrounded by an infinite domain of material and that this material has the properties of  $\sigma^b$  (as shown in Figure 11). Figure 11 shows two possible approximations

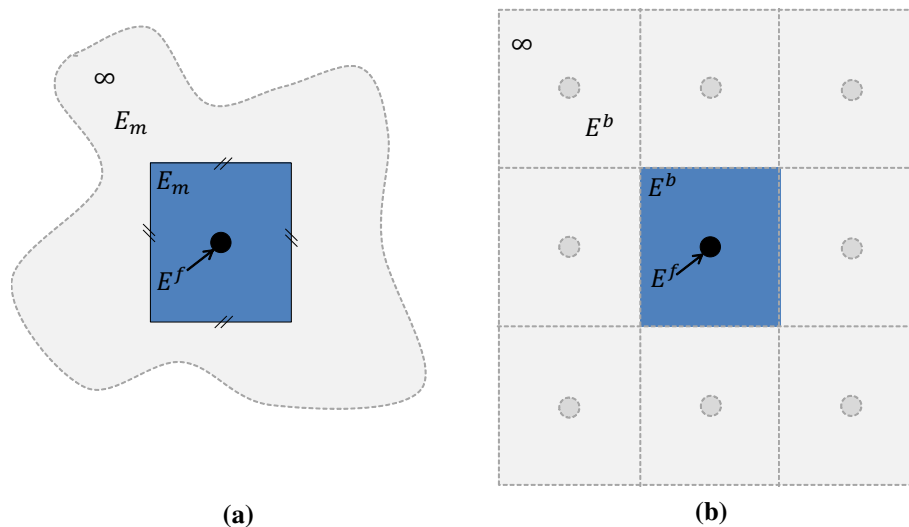


Figure 11: Two assumptions for the far field properties used to determine inclusion response a) an Eshelby type assumption b) a self-consistent type assumption which will be used in this work

for the matrix properties far from the inclusion of interest. Figure 11a assumes that these far field properties are that of the matrix, and thus the inclusion stress will be a function of  $E_m$ . Figure 11b assumes that the far field properties are those of the composite, and thus the inclusion stress will be a function of  $E^b$ . The later is a self consistent type assumption. The assumption in Figure 11b will be used for this work, as it takes into account surrounding microstructure. From this approximation,  $K_t^*$  is defined as the ratio of the peak matrix stress ,which occurs at the filler matrix interface for



dilute microstructure, to the stress far from the inclusions,  $\sigma^b$ . The stress concentration factor is expressed then as

$$K_t^* = \frac{\sigma_{yy}^{\text{peak}}}{\sigma_{yy}^b}, \quad (12)$$

where the  $y$ -direction is the loading direction. It is then noted that the peak stress occurs at the largest  $y$  coordinate of the inclusion at the interface between the filler and matrix (point  $a$  seen in Figure 12). At this point the force continuity condition holds; this condition [22] is expressed as,

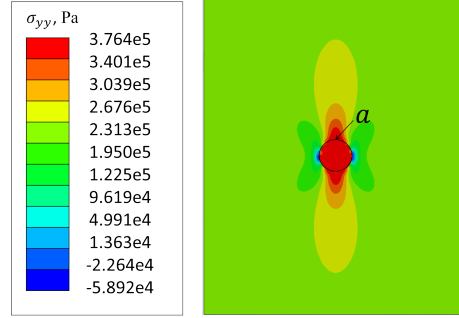


Figure 12: Real normal stress in the  $y$  for a single particle in a dilute system (volume fraction of 1%). Contour is for a frequency of  $1 \times 10^{-2}$  (1/second)

$$\sigma_{a+}^m \cdot \mathbf{n}_{a+} = \sigma_{a-}^f \cdot \mathbf{n}_{a-}, \quad (13)$$

where  $\mathbf{n}$  is a unit normal vector,  $a+$  and  $a-$  represent points just above (+) and below(-) point  $a$  as shown in Figure 13. It is also noted that in an Eshelby problem the inclusion stress is considered constant, an assumption which will be adopted here. The validity of this assumption is illustrated in both Figure 7a and Figure 12. Thus,

$$\sigma_{a-}^f = \sigma^f. \quad (14)$$

Since  $\mathbf{n}_{a+}$  and  $\mathbf{n}_{a-}$  are equal, substituting Equation 14 into Equation 13 and using only the  $\sigma_{yy}$  components gives

$$\sigma_{yy(a+)}^m = \sigma_{yy}^f. \quad (15)$$

Since  $a+$  is the location of peak  $yy$  stress,  $\sigma_{yy(a+)}^m = \sigma_{yy}^{\text{peak}}$ , and thus the complex stress concentration factor, resulting from inserting Equation 15 into Equation 12, is given by

$$K_t^* = \frac{\sigma_{yy}^f}{\sigma_{yy}^b}, \quad (16)$$

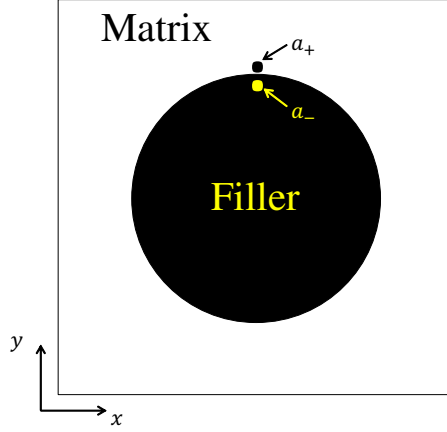


Figure 13: point  $a+$  and  $a-$  across matrix/filler interface at which continuity is considered

where both  $\sigma_{yy}^f$  and  $\sigma_{yy}^b$  are complex values. The real and imaginary parts of  $K_t^*$  are plotted against frequency as shown in Figure 14. This Figure shows that reasonable values of real  $K_t$  between 1.0 and 2.0 are estimated. Note that the stress concentration factor for a rigid inclusion is 1.478 [24]. However for imaginary values of  $K_t$  values between zero and negative numbers are estimated, both of which are not physically consistent with the problem at-hand. The effect of the imaginary stress concentration factor is thus neglected and  $K_t^*$  becomes

$$K_t^* = \Re\left(\frac{\sigma_{yy}^f}{\sigma_{yy}^b}\right) + 1i, \quad (17)$$

where  $\Re(\cdot)$  represents the real part of a function  $(\cdot)$ . Therefore, the average stress can be partitioned into real and imaginary parts as

$$\Re(\bar{\sigma}_{yy}) = (1 - w_1)\Re(\sigma_{yy}^b) + w_1\Re(K_t^* \sigma_{yy}^b), \quad (18)$$

$$\Im(\bar{\sigma}_{yy}) = \Im(\sigma_{yy}^b), \quad (19)$$

where  $\Im(\cdot)$  represents the imaginary part of a function  $(\cdot)$ . The stress real stress concentration factor shown in Figure 14 and the assumption that imaginary stress concentration factor is unity, agrees reasonably well with finite element calculations of  $K_t^*$  for a low volume fraction, especially at high frequencies. Overall, this model for  $K_t^*$  captures the general trend seen from finite element results, that the real part of  $K_t^*$  exceeds the imaginary part across the frequency spectrum. The

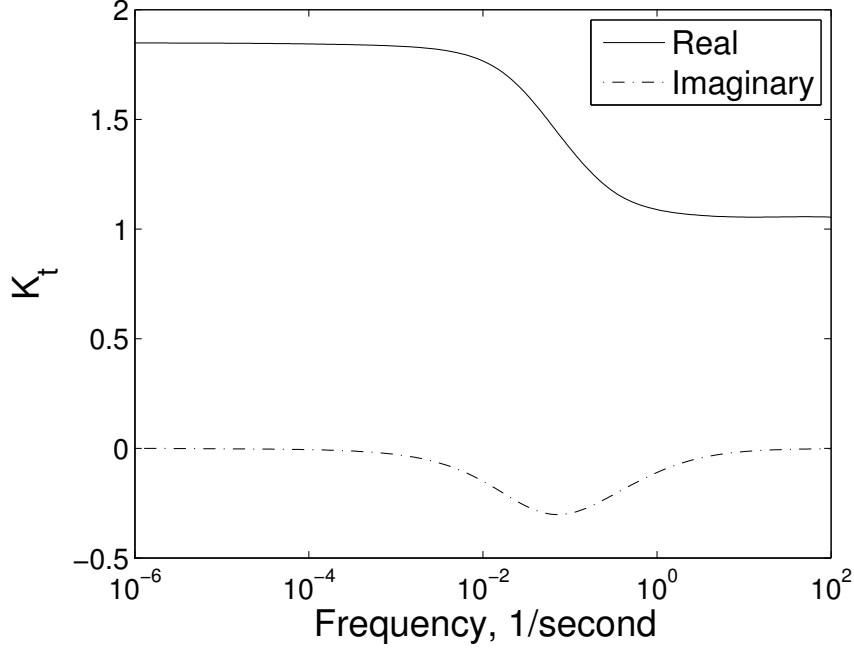


Figure 14: complex tensile stress concentration factor as a function of frequency for 20% volume fraction

filler stress, needed in Equation 16, is again determined using the self consistent assumption

$$\sigma^f = \hat{\sigma}^{\text{inc,MT}}(\mathbf{S}, E^b, \nu^b, E^f, \nu^f), \quad (20)$$

where the  $\hat{\cdot}$  denotes a function,  $\hat{\sigma}^{\text{inc,MT}}$  is the inclusion stress predicted by Mori-Tanaka, and  $E^b$  and  $\nu^b$  the Young's modulus and Poisson's ratio of the composite predicted either by Mori-Tanaka or Halpin-Tsai. Note that Mori-Tanaka is based on Eshelby's solution, which gives direct access to inclusion (i.e. filler) stress and strain. Inclusion response is not readily provided by the Halpin-Tsai model and thus Mori-Tanaka is used to determine filler stress regardless of the base model. This is somewhat of an inconsistency for 2D analysis but is accepted with the purpose of including the Halpin-Tsai model in this study, because it is the preferred model in many situations and by many modelers. For 3D, the base model will always be Mori-Tanaka, remedying this inconsistency. Also a general approximation is that  $\nu^b = \nu^m + 0i$ , which is an assumption that is not strictly true but generally results in negligible error.

## 7. Implementation

### 7.1. Subcell Model

To implement the model extension shown in Section 6, an average aspect ratio is determined for each subcell as

$$\mathcal{R} = \frac{1}{V_{\text{subcell}}} \sum_{c=1}^{N_c} \mathcal{R}_c V_c, \quad (21)$$

where  $c$  is an index for each filler cluster,  $N_c$  the number of filler clusters and  $V_{\text{subcell}}$  and  $V_c$  are the volume of the subcell and each filler cluster respectively. The aspect ratio for each cluster  $\mathcal{R}_c$  is determined, in 2D, as

$$\mathcal{R}_c = \frac{l_{\text{major}}}{l_{\text{minor}}}, \quad (22)$$

where  $l_{\text{major}}$  is the length of the major axis of a filler cluster, and  $l_{\text{minor}}$  is the length of the minor axis. The major axis is considered to always be in the loading direction. These lengths are measured as the difference between the maximum and minimum coordinates of a cluster in each direction.

Also for implementation, the form of  $w_1$  must be determined. Again,  $w_1$  represents the volume fraction of matrix with an average stress of  $K_t^* \sigma_{yy}^b$ . This is in general difficult to determine exactly, but it can be estimated as a function of the three main physical descriptors discussed above

$$w_1 \equiv \hat{w}_1(c_f, \zeta, \mathcal{R}), \quad (23)$$

where  $\zeta$  is the percentage of filler particles interacting. In this work, only a simple form of  $w_1$  will be posed, but further extensions will be described in Section 10. One of the simplest forms is

$$w_1 = \zeta. \quad (24)$$

The power of this assumption is that when only one filler particle is present,  $\zeta = 0$  and the extended model degrades to the base model. This makes physical sense, in that, for a single inclusion the region where stress is  $K_t^* \sigma_{yy}^b$  is only a single point (with a volume fraction of zero). Also  $w_1$  in Equation 24 increases as the number of particles interacting increases and so does the physical volume with an elevated stress.

However, one detail of the assumption in Equation 24 needs to be further addressed. This detail is that  $\zeta$  can take on a range of values as

$$\{\zeta \in \mathbb{R} \mid 0 \leq \zeta \leq 1\}. \quad (25)$$

Since  $w_1$  cannot exceed the volume fraction of the matrix, the average stress must be recast as

$$\bar{\sigma} = \begin{cases} (1 - w_1)\sigma^b + w_1\sigma^{int}, & \text{if } w_1 \leq (1 - c_f) \\ (1 - c_f)\sigma^{int} + c_f\sigma^f, & \text{if } w_1 > (1 - c_f) \end{cases} \quad (26)$$

where  $\sigma^f$  is the filler/inclusion stress.

To determine  $\zeta$ , a 10 x 10 voxel subcell is considered. First, the number of clusters is determined using the MATLAB function, `BWLABEL`, each cluster getting a label as shown in Figure 15. The

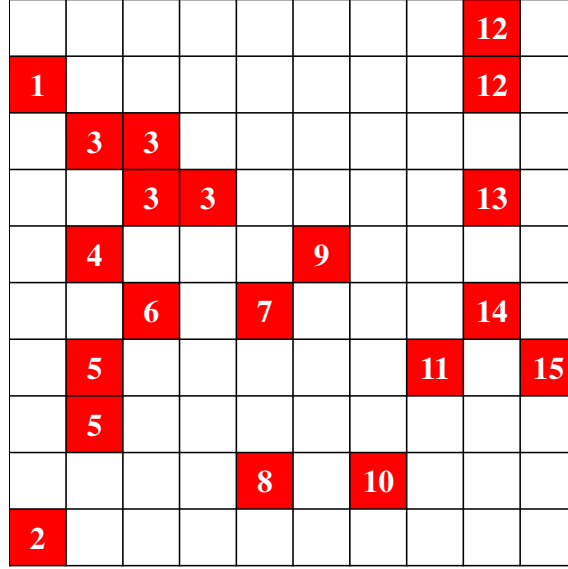


Figure 15: cluster labels for voxel subcell image

algorithm for  $\zeta$  searches through a list of filled voxels; if a filled voxel is within an integer distance,  $dr$ , of another filled voxel, then the current voxel is considered to be interacting as shown by the grey voxels in Figure 16. Then  $\zeta$  is determined as

$$\zeta = \frac{\text{number of filled voxels interacting}}{\text{number of filled voxels}}. \quad (27)$$

A cluster interacting with itself, such as the merlon structure in Figure 16d, is considered interacting since a high stress region will exist between merlons. Assuming a constant aspect ratio, subcells of random and single particles are considered, where  $\zeta$  is calculated for each subcell. The results are shown in Figure 10. It can be seen that the model captures both the single inclusion response as well as the drop in  $\tan \delta$  due to interactions in random microstructures. It is also noted that

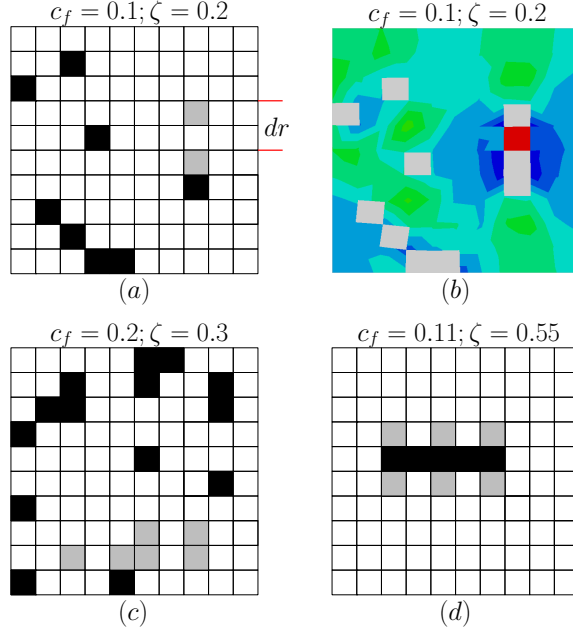


Figure 16: a) an example of 10x10 subcells with 10% volume fraction, the grey particles are considered *interacting*,  $dr = 2$  voxels and the percentage of interacting particles,  $\zeta$ , is given b) the real normal stress at a frequency of  $1 \times 10^{-2}$  (1/second) in the  $y$  direction for the microstructure in a), the interaction stress between grey voxels is shown c) an example of 10x10 subcells with 20% volume fraction d) self-interaction of a cluster with a merlon structure

$dr$  was set to a value of 2 voxels for the results shown in Figure 10. The value of  $dr$  is considered somewhat of a fitting parameter, but, based on subcell DNS, a value of 2 or 3 seems reasonable. Further finite element or molecular dynamics studies (such as those in [25]) could determine more exact values for  $dr$ .

## 7.2. RVE Cell Model

Using the micromechanics model extension outlined in the previous sections, a 2D RVE microstructure is considered as shown in Figure 3a. The microstructure was constructed using a 2D kinetic Monte Carlo algorithm explained in Appendix A. This structure is meant to be somewhere between a purely random structure and an array of single inclusion subcells. The response of both base models with the addition of the proposed model extension are shown in Figure 17. It can be seen from Figure 17 that both the extended Halpin-Tsai and Mori-Tanaka models agree well with DNS results. It can also be seen that the extended models are an improvement over the

prediction made by the original Halpin-Tsai model.

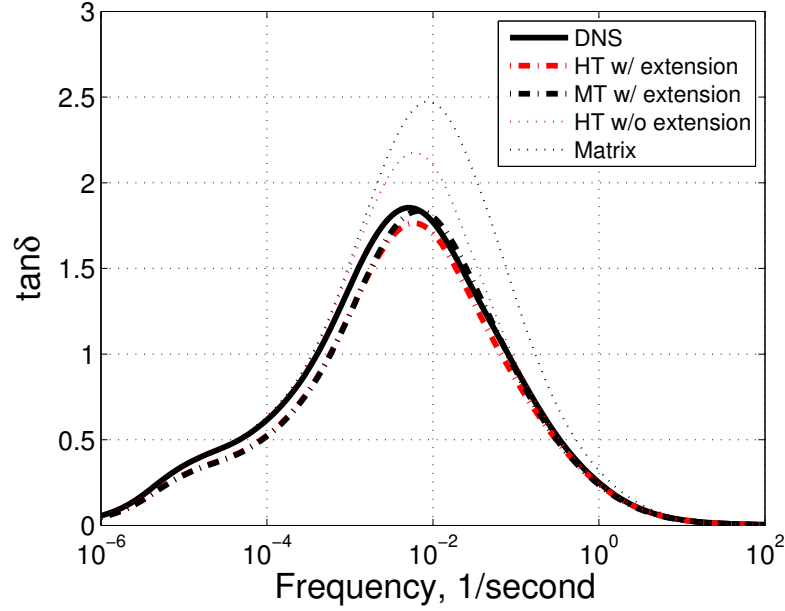


Figure 17: results using the model extension are compared to DNS results for a 2D system. The response from the original Halpin-Tsai model and pure matrix are shown for comparison

## 8. Three Dimensional Modeling

It is known that models of viscoelastic systems in 2D and 3D generally yield different results. In some circumstances this discrepancy is due to different percolation limits in 2D and 3D. While more frequently this discrepancy can be attributed to the fact that area fraction in 2D and volume fraction in 3D are not equivalent. In plane strain analysis, as was presented previously, area fraction and volume fraction were identical, but this is rarely the case for real microstructures. For example, a circular inclusion with a fixed radius in 2D may have an area fraction of 20%; a spherical inclusion with the same radius in 3D will have a volume fraction of 6.7%. Thus the viscoelastic response of the 2D system with an area fraction of 20% will resemble the response of a 3D system with a volume fraction of 6.7%. The mapping between 2D area fraction and 3D volume fraction is straight forward based on simple geometry for a circle and sphere respectively; however, a mapping of this type for an arbitrary and complex microstructure would be very difficult to determine analytically.

Due to this difficulty, the 2D model, which was useful for comparing to tractable DNS results, is less useful for making predictions that can be compared to 3D experiential data; thus, a 3D model is explored here. To cast the model implemented in Section 7 into a three dimensional form, a 3D microstructure was generated. The 3D microstructure was generated by randomly placing filler particles in a 100 x 100 x 100 voxel matrix as is shown in Figure 18. While the previous 2D work

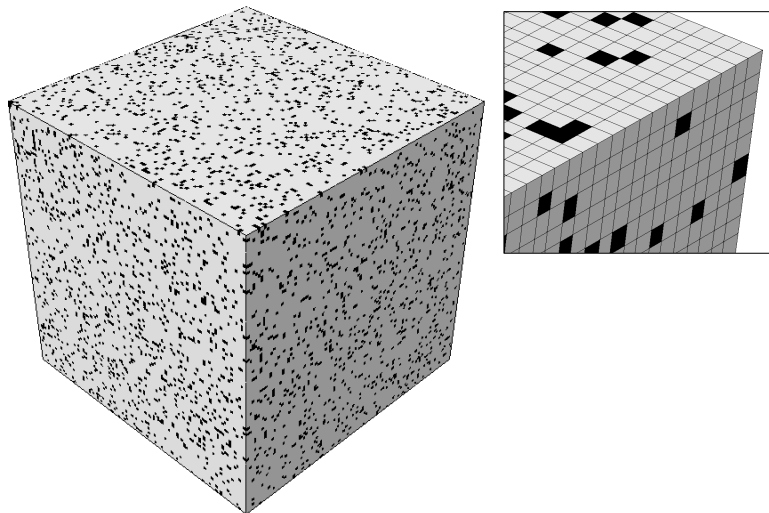


Figure 18: 3D random microstructure, black voxels are filler, white voxels matrix, inset shows mesh detail

extends to 3D without any modification to the proposed theory, a few implementation aspects need clarified in the context of 3D analysis. The first is the base model itself. Mori-Tanaka is based on the Eshelby tensor, which is formulated in 3D. Halpin-Tsai on the other hand relies solely on a 2D aspect ratio. Thus, only the Mori-Tanaka model will be used in 3D. The form of the Eshelby tensor used considers each inclusion to be a prolate spheroid with two equal minor axes and one longer major axis and is given in [9]. The major axis was considered to be aligned with the load, as was the case in 2D. To characterize this shape, the aspect ratio was determined as:

$$\mathcal{R} = \frac{l_{\text{major}}}{\text{mean}[l_{\text{minor1}}, l_{\text{minor2}}]}, \quad (28)$$

where  $l_{\text{major}}$  is the length of the major axis of a filler cluster. The lengths  $l_{\text{minor1,2}}$  represent the length of each minor axis respectively. The aspect ratio of every cluster in a subcell was calculated and volume-averaged as in Equation 22 in 2D.



The computational cost savings of the model extension become evident in 3D analysis. For illustration purposes the author has run a 3D viscoelastic calculations for a 80 x 80 x 80 mesh which considers 50 frequencies. Using 64 processors on the Quest computing cluster [26] this simulation took approximately 15 hours. For the proposed model with a 100 x 100 x 100 microstructure the simulation took approximately 5 minutes using 2 Intel <sup>®</sup>Core <sup>™</sup>i7-950, 3.07GHz processors. Approximately half of this time was spent calculating homogenized properties using the extended micromechanics model and the other half in the finite element calculation. The speedup is attributed solely to the fact that the homogenization reduces the size of the finite element calculation. For the 100 x 100 x 100 microstructure only a 10 x 10 x 10 finite element mesh was needed using the proposed homogenization procedure, resulting in substantial speedup. The proposed model extension has substantially increased the speed of calculations of viscoelastic properties for 3D microstructures, making the simulation of large RVE scale microstructure possible in 3D and smaller domain sized calculations tractable without advanced computer resources.

## 9. Three Dimensional Modeling with Interphases

It has been shown in [2] [27] [25] [28] [29] [30] [31] [32] that the properties of many polymers differ from that of the bulk matrix in regions near fillers. These regions are referred to as interphase regions. The effect of fillers on matrix properties is predominant in nanocomposites where the surface area is substantial [27]. The volume fraction and average thickness of the interphase region has been investigated by the author using course grain molecular dynamics simulations for polymer chains confined between non-attractive spherical nanoparticles [25]. It was found that the interphase volume fraction can be expressed as a function of filler volume fraction as

$$c_{IP} = (1 - c_f)[1 - \exp(-3.07c_f)]. \quad (29)$$

It was also determined that the interphase thickness  $d_{IP}$  can be directly estimated from  $c_{IP}$ . For relatively dilute filler clusters, the interphase thickness was expressed as

$$c_{IP}L_{\text{sim}}^3 = M_{NP}4\pi[(R_F + d_{IP})^3 - R_f^3]/3 \quad (30)$$

where  $L_{\text{sim}}$  is the length of the side of a simulation box,  $M_{NP}$  is the number of filler nanoparticles and  $R_f$  is the bare radius of the nanoparticles. Using Equation 29 the volume fraction of the interphase region can be incorporated into an expression for average composite stress. The volume

fraction of the interphase will from here on be referred to as  $\omega_2$ . The 3D average composite stress with an IP region is then expressed as

$$\bar{\sigma} = \begin{cases} (1 - w_1)\sigma^b + (w_1 - w_2)\bar{\sigma}^{int}(\mathbf{L}^b) + w_2\bar{\sigma}^{int}(\mathbf{L}^{IP}), & \text{if } w_1 \geq w_2 \\ (1 - w_2)\sigma^b + (w_1)\bar{\sigma}^{int}(\mathbf{L}^{IP}) + (w_2 - w_1)\bar{\sigma}^{IP}(\mathbf{L}^{IP}), & \text{if } w_2 > w_1. \end{cases} \quad (31)$$

For simplicity it has been assumed that  $K_t$  is the same as used for analysis without IP and that neither  $w_1$  or  $w_2$  exceeds the volume fraction of the matrix  $(1 - c_f)$ . The expressions in Equation 31 assume that the IP and interaction regions are concentric. From Equation 31, the response of 3D the system can be determined if the properties of the interphase region are known. The constitutive expression for the IP region will be expressed as a volume-average over the IP region as

$$\mathbf{L}^{IP} = \frac{1}{\Omega_{IP}} \int_{\Omega_{IP}} \tilde{\mathbf{L}}^{IP}(\mathbf{x}) d\Omega, \quad (32)$$

where  $\Omega_{IP}$  is the IP volume, and  $\tilde{\mathbf{L}}^{IP}$  is a local quantity of interphase material properties as a function of distance  $\mathbf{x}$  from the filler surface.

Two simple models for the interphase region are examined here. Figure 19 shows the variation in peak  $E'$  and  $E''$  using a linear and exponential transition between the filler and matrix properties over the IP region. The expressions for  $E^*$  with a linear and exponential transition over the width

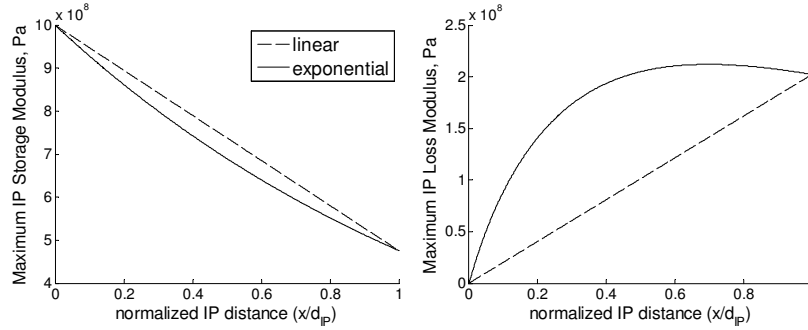


Figure 19: Linear and exponential transition of IP properties over the IP thickness

of the interphase are given receptively in

$$E_{IP}^* = E_f + (E_m^* - E_f)\hat{x}, \quad (33)$$

$$E_{IP}^* = E_f \left( \frac{E_m^*}{E_f} \right)^{\hat{x}}, \quad (34)$$

where  $\hat{x}$  is a normalized distance,  $x/d_{IP}$ . Equation 32 was evaluated using both Equation 33 and 34 for  $\tilde{\mathbf{L}}^{IP}$  and used in a 3D simulation of  $\tan \delta$  for a random microstructure. The results are shown in Figure 20. These results are also compared to the  $\tan \delta$  of the IP region alone, as

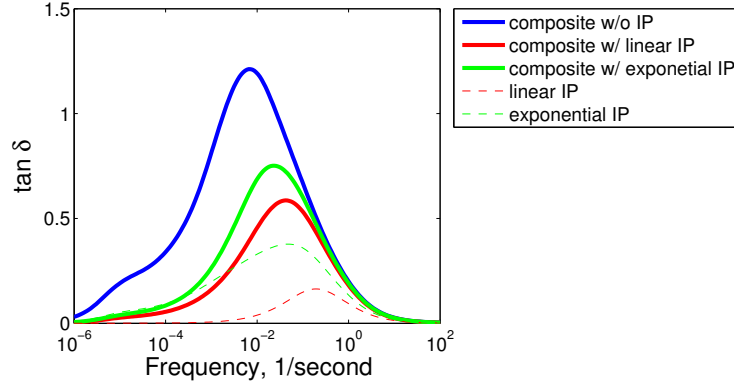


Figure 20: Effect of an IP region on  $\tan \delta$  for a 3D random microstructure. Properties of the IP region are shown for reference

indicated by dashed lines in Figure 20. It is shown in Figure 20, that the presence of an IP region reduces  $\tan \delta$  and that the linear IP region reduces  $\tan \delta$  more than the exponential region.

The goal of the 3D model is to make predictions which can be translated to materials design. Thus, a brief study of the IP thickness is shown here. This is by no means the only variable which can be explored but showcases the type of parametric studies possible in a short timespan with a fast model. For cases where the IP properties vary exponentially (i.e. Equation 34), the IP distance was calculated for each subcell. The addition of filler reduces  $\tan \delta$  and the presence of an exponential IP region further decreases  $\tan \delta$  response. As was shown in [2], it is often desirable to have  $\tan \delta$  as high as possible in certain frequency ranges to maximize performance of systems such as tire materials. Thus, it would also be desirable to know how much  $d_{IP}$  should be reduced to see a substantial increase in  $\tan \delta$ . Figure 21 shows the response of peak  $\tan \delta$  to decreases in IP thickness. For this study,  $d_{IP}$  is determined for each subcell using Equation 30, then reduced by varying amounts. Exponentially varying IP properties were also used for the study in Figure 21. The average IP thickness was  $d_{IP} = 0.13$  voxels, which showcases that the model can account for a non-integer voxel IP thicknesses. It can be seen that the effect of IP distance on peak  $\tan \delta$  becomes nonlinear at approximately 80% of the predicted  $d_{IP}$ . However, it is shown that to increase peak

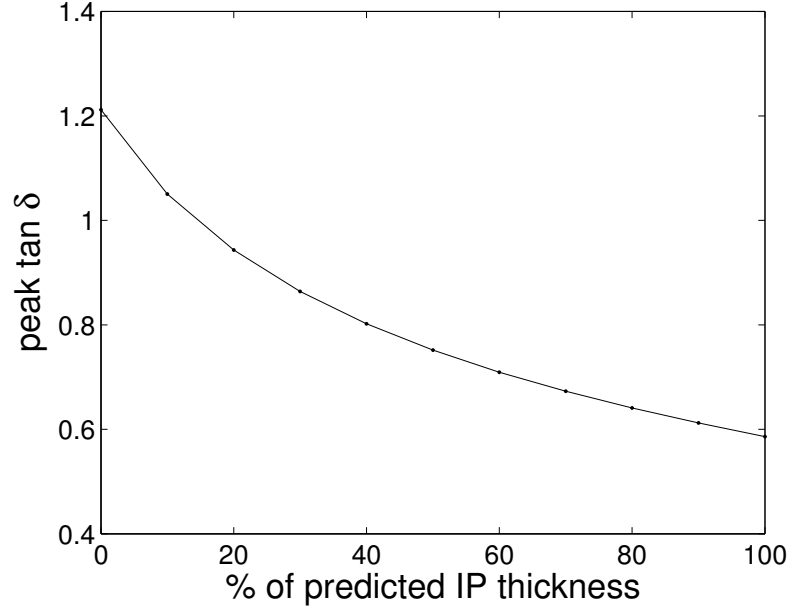


Figure 21: peak  $\tan \delta$  as a function of decreasing IP thickness; IP properties are exponentially varying across the IP region

$\tan \delta$  to within 20 % of the value without an interphase region would require an 80% reduction in  $d_{IP}$  (i.e. 20% of  $d_{IP}$ ). A detailed consideration of the processing and functionalization of the filler particles would reveal if this reduction is possible.

Another study was also performed showing the effect of shifting the frequency of  $\tan \delta$  in the IP region. All  $\tan \delta$  values were uniformly shifted a given number of decades. The results are shown in Figure 24. It can be seen that a shifted IP with no reduction in  $\tan \delta$  amplitude results in little change in composite properties. In the 2D work of Deng et al. [20], a larger effect of shifting IP properties was shown. They studied a minimum IP volume fraction of 24.4% where as in the current study the average IP volume fraction is 10.8% which could account for the reduced effect. From these two studies, the following conclusions can be made. First, the effect of IP thickness is nonlinear; the effects of reducing IP thickness are amplified for large percentage reductions. Second, the IP thickness would need to be reduced 80% to achieve 80% of the composite properties seen without an IP region. Third, if the IP region is less lossy than the matrix, then the maximum value of  $\tan \delta$  for a given volume fraction is shown in Figure 20 as the  $\tan \delta$  with no IP. Further increase

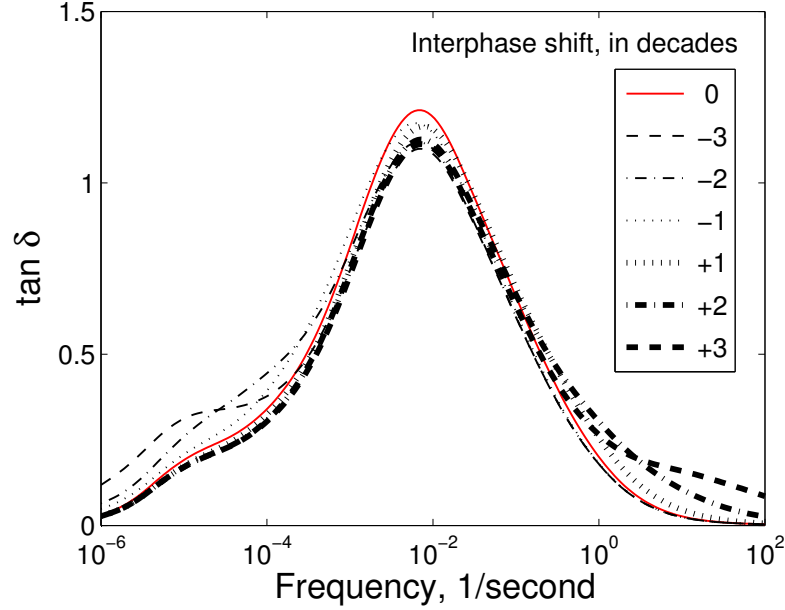


Figure 22: Effect of shifting the frequencies of IP properties on 3D  $\tan \delta$  responses. Numbers in the legend represent the number of decades IP  $\tan \delta$  was shifted, with (+) being a shift to higher frequencies

in  $\tan \delta$  would require changing variables other than IP thickness. Fourth, a linear gradient in the IP region reduces  $\tan \delta$  more than an exponential gradient, and fifth, amplitude changes in IP  $\tan \delta$  have much more of an effect on composite response than frequency shifts, for low IP volume fractions of 10% or less. These results would hopefully give materials designers some guidance into how to modify the interphase properties, or alternatively inform designers as to the possibility of increasing  $\tan \delta$  by means of IP property changes, perhaps a lower volume fraction would be required to meet design goals.

It should be noted that the IP properties used here are very simple, and much more complex forms exist. For example, the author has chosen the IP properties to vary from that of the filler to that of the matrix. However, it is known that there will be a jump in properties between filler and matrix. It was not the goal of this work to characterize this jump, and thus the author uses the simple form shown in Figure 19 as an example. It also can be shown that the IP properties are a function of not only the distance from a filler but also the effects of filler-filler interactions such that  $\tilde{\mathbf{L}}^{IP} = \tilde{\mathbf{L}}^{IP}(\mathbf{x}, \zeta)$ . This dependence could easily be included in the proposed model extension

(as  $\zeta$  is available) but was not considered here. Another use of the proposed model is to leave  $\mathbf{L}^{IP}$  as an unknown and compare it to experimental data. From this comparison the value of  $\mathbf{L}^{IP}$ , which showed good agreement between experimental results and the model, could be considered the appropriate value of interphase properties. Thus, the proposed model could be used to back out interphase properties of a polymer, (as was done in [20]) which may be difficult to access experimentally, much like researchers in MicroElectroMechanical Systems (MEMS) back out microscale materials properties based on the response of micro-beams. If the determined properties vary for different region of the microstructure using  $\tilde{\mathbf{L}}^{IP} = \tilde{\mathbf{L}}^{IP}(\mathbf{x})$ , then a dependence of IP properties on a filler-filler interaction is evident, and the form  $\tilde{\mathbf{L}}^{IP} = \tilde{\mathbf{L}}^{IP}(\mathbf{x}, \zeta)$  should be considered. It is possible that the appropriate form of  $\tilde{\mathbf{L}}^{IP}(\mathbf{x}, \zeta)$  could be backed out as well. The determination of this dependence would increase knowledge of the polymer system, which showcases the usefulness of the proposed model extension not only for design but also for discovery.

## 10. Summary and Conclusions

A model extension to the traditional Mori-Tanaka and Halpin-Tsai equations was proposed here. This extension captured effects of stress risers near interacting filler particles to allow for larger subcells when homogenizing an RVE scale cell. The model extension agreed well with DNS calculations in 2D for subcells with a medium number of filler clusters. 3D predictions showed the effect of interphase regions and showcased the substantial increase in computational speed over direction simulations.

The form of the interaction volume expression was based on a very simple formulation. Future work may express this term based on more detailed microstructural metrics such as, two point correlation function or surface area of the filler clusters. This work was meant to characterize  $\tan \delta$ , which can be determine from a one dimensional (1D) loading. Thus, the expressions for average stress were reduces to 1D as well, which greatly simplified the determination of stress concentration factor. If three dimensional properties are of interest, a more sophisticated method would be needed to determine  $K_t$  for 3D load states. Recent work by the author and his collaborators in generalized continuum mechanics [33] [34] could offer a method to determine 3D  $K_t$ , where extra degrees of freedom account for subcell scale stress states.

Overall, the hope is that the model extension proposed here will allow materials designers to explore complex elastomeric systems in more detail, resulting in better, safer and more efficient

materials and discoveries of complex micro or nanoscale mechanism, which were previous out of the scope of current modeling procedure.

## Acknowledgement

The support of this research by National Science Foundation (NSF) is gratefully acknowledged. We would also like to thank Brendan Abberton and Wylie Stroberg for their contribution of the kinetic Monte Carlo code.

## Appendix A. Kinetic Monte Carlo

The 2D microstructure was generated using a Monte Carlo simulation based on the 2D kinetic Ising model. The details of a 2D Ising model are given in [35]. The model initializes a voxelized system with a given filler volume fraction. The Monte Carlo method will exchange matrix and filler voxels in such a way that volume fraction is conserved. The model calculates the energy change,  $\Delta E$ , due to exchanging a voxel. If the  $\Delta E < 0$ , then the change is accepted. If  $\Delta E > 0$ , then the exchange is accepted based on the probability  $P = \exp(-\Delta E/k_b T)$ , where  $k_b$  is Boltzmann's constant and  $T$  the system temperature. The energy is calculated as  $E = -J \sum_{\langle i,j \rangle} S_i S_j$  where  $\langle i,j \rangle$  is the sum over the nearest neighbor voxels  $i,j$  and  $S_{i,j}$  are spins mapped from filler concentration,  $C^f$ . This mapping is  $S_i = 2C_i^f - 1$ . The concentration is determined by  $C(T) = C_c \pm \{1 - [\sinh(2J/k_b T)]^{-4}\}^{1/8}$  where  $J$  is approximated as  $J = k_n T / 0.4407$  and  $C_c$  a critical concentration.

The aforementioned Monte Carlo simulation will not necessarily represent the physics of a filled elastomer system; however, it will give a microstructure which is less ordered than periodic single particles but more morphologically diverse than randomly distributed filler voxels. Ideally, this microstructure will be determined based on imaging as was performed by Deng et al. [20], but this type of imaging was beyond this scope of this work.

## References

- [1] V. Mittal, Optimization of polymer nanocomposite properties, Wiley. com, 2009.
- [2] M.-J. Wang, Effect of polymer-filler and filler-filler interactions on dynamic properties of filled vulcanizates, Rubber Chemistry and Technology 71 (3) (1998) 520–589.

- [3] I. D. Aiken, J. M. Kelly, F. F. Tajirian, Mechanics of low shape factor elastomeric seismic isolation bearings, Vol. 89, Earthquake Engineering Research Center, College of Engineering, University of California, 1989.
- [4] C. W. Roeder, J. F. Stanton, Elastomeric bearings: state-of-the-art, Journal of Structural Engineering 109 (12) (1983) 2853–2871.
- [5] T. V. Duncan, Applications of nanotechnology in food packaging and food safety: Barrier materials, antimicrobials and sensors, Journal of colloid and interface science 363 (1) (2011) 1–24.
- [6] M. T, T. K, Average stress in matrix and average elastic energy of materials with misfitting inclusions, acta metallurgica 21 (1973) 571.
- [7] A. JE, J. Halpin, Primer on composite materials: analysis, Technomic, 1969.
- [8] J. D. Eshelby, The determination of the elastic field of an ellipsoidal inclusion, and related problems, Proceedings of the Royal Society of London. Series A. Mathematical and Physical Sciences 241 (1226) (1957) 376–396.
- [9] J. Qu, M. Cherkaoui, Fundamentals of Micromechanics of Solids, John Wiley & Sons, Inc, 2006.
- [10] C. L. Tucker III, E. Liang, Stiffness predictions for unidirectional short-fiber composites: review and evaluation, Composites science and technology 59 (5) (1999) 655–671.
- [11] R. Hill, Theory of mechanical properties of fibre-strengthened materials: I. elastic behaviour, Journal of the Mechanics and Physics of Solids 12 (4) (1964) 199–212.
- [12] L. Brinson, W. Lin, Comparison of micromechanics methods for effective properties of multi-phase viscoelastic composites, Composite Structures 41 (3) (1998) 353–367.
- [13] K. Putz, R. Krishnamoorti, P. F. Green, The role of interfacial interactions in the dynamic mechanical response of functionalized swnt–ps nanocomposites, Polymer 48 (12) (2007) 3540–3545.
- [14] X. L. Ji, J. K. Jing, W. Jiang, B. Z. Jiang, Tensile modulus of polymer nanocomposites, Polymer Engineering & Science 42 (5) (2002) 983–993.



- [15] G. Li, Y. Zhao, S.-S. Pang, Four-phase sphere modeling of effective bulk modulus of concrete, *Cement and Concrete Research* 29 (6) (1999) 839–845.
- [16] A. A. Gusev, S. A. Lurie, Loss amplification effect in multiphase materials with viscoelastic interfaces, *Macromolecules* 42 (14) (2009) 5372–5377.
- [17] H. Liu, L. C. Brinson, A hybrid numerical-analytical method for modeling the viscoelastic properties of polymer nanocomposites, *Journal of applied mechanics* 73 (5) (2006) 758–768.
- [18] Y. Song, Q. Zheng, Application of two phase model to linear viscoelasticity of reinforced rubbers, *Polymer* 52 (3) (2011) 593–596.
- [19] L. Mishnaevsky Jr, Micromechanical analysis of nanocomposites using 3D voxel based material model, *Composites Science and Technology* 72 (10) (2012) 1167–1177.
- [20] H. Deng, Y. Liu, D. Gai, D. A. Dikin, K. W. Putz, W. Chen, L. Catherine Brinson, C. Burkhart, M. Poldneff, B. Jiang, et al., Utilizing real and statistically reconstructed microstructures for the viscoelastic modeling of polymer nanocomposites, *Composites Science and Technology* 72 (14) (2012) 1725–1732.
- [21] C. M. Breneman, L. C. Brinson, L. S. Schadler, B. Natarajan, M. Krein, K. Wu, L. Morkowchuk, Y. Li, H. Deng, H. Xu, Stalking the materials genome: A data-driven approach to the virtual design of nanostructured polymers, *Advanced Functional Materials*.
- [22] T. Belytschko, B. Moran, W. K. Liu, K. Elkhodary, *Nonlinear finite element analysis for continua and structures*, 2nd Edition, Wiley, in press.
- [23] D. Simulia, *Abaqus 6.11 theory manual*, Providence, RI, USA: DS SIMULIA Corp.
- [24] P. WD, *Petersons stress concentration factors*, New York: Wiley, 1997.
- [25] Y. Li, M. Kröger, Dynamic structure of unentangled polymer chains in the vicinity of non-attractive nanoparticles, *Soft Matter*.
- [26] Quest, Northwestern University, <http://www.it.northwestern.edu/research/adv-research/hpc/quest/>.

- [27] T. Ramanathan, A. Abdala, S. Stankovich, D. Dikin, M. Herrera-Alonso, R. Piner, D. Adamson, H. Schniepp, X. Chen, R. Ruoff, et al., Functionalized graphene sheets for polymer nanocomposites, *Nature Nanotechnology* 3 (6) (2008) 327–331.
- [28] K. I. Winey, R. A. Vaia, Polymer nanocomposites, *MRS bulletin* 32 (04) (2007) 314–322.
- [29] P. Akcora, S. K. Kumar, V. Garca Sakai, Y. Li, B. C. Benicewicz, L. S. Schadler, Segmental dynamics in pmma-grafted nanoparticle composites, *Macromolecules* 43 (19) (2010) 8275–8281.
- [30] G. N. Toepferwein, N. C. Karayiannis, R. A. Riggelman, M. Krger, J. J. de Pablo, Influence of nanorod inclusions on structure and primitive path network of polymer nanocomposites at equilibrium and under deformation, *Macromolecules* 44 (4) (2011) 1034–1045.
- [31] J. Torres, P. Nealey, J. De Pablo, Molecular simulation of ultrathin polymeric films near the glass transition, *Physical Review Letters* 85 (15) (2000) 3221.
- [32] Y. Li, M. Kröger, W. K. Liu, Nanoparticle effect on the dynamics of polymer chains and their entanglement network, *Physical Review Letters* 109 (11) (2012) 118001.
- [33] K. I. Elkhodary, M. Steven Greene, S. Tang, T. Belytschko, W. K. Liu, Archetype-blending continuum theory, *Computer Methods in Applied Mechanics and Engineering*.
- [34] M. S. Greene, Mechanics and physics of solids, uncertainty, and the archetype-genome exemplar, Ph.D. thesis, Northwestern University (2012).
- [35] L. D. Landau, E. M. Lifshitz, *Statistical Physics, Part 1*, 3rd Edition, Vol. 5, Butterworth-Heinemann, 1980.